

 Open access • Journal Article • DOI:10.3847/1538-4357/ABD407

An Improved Measurement of the Secondary Cosmic Microwave Background Anisotropies from the SPT-SZ + SPTpol Surveys — [Source link](#)

Christian L. Reichardt, S. Patil, P. A. R. Ade, Adam Anderson ...+90 more authors

Institutions: University of Melbourne, Cardiff University, Fermilab, National Institute of Standards and Technology ...+24 more institutions

Published on: 14 Feb 2020 - [arXiv: Cosmology and Nongalactic Astrophysics](#)

Related papers:



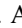

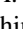



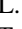











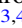

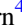

- [A measurement of secondary cosmic microwave background anisotropies from the 2500-square-degree SPT-SZ survey](#)
- [Matplotlib: A 2D Graphics Environment](#)
- [The Simons Observatory : Science goals and forecasts](#)
- [Improved constraints on cosmic microwave background secondary anisotropies from the complete 2008 South Pole Telescope data](#)
- [A measurement of secondary cosmic microwave background anisotropies with two years of South Pole Telescope observations](#)

Share this paper:    

View more about this paper here: <https://typeset.io/papers/an-improved-measurement-of-the-secondary-cosmic-microwave-27wpe9pdcw>



An Improved Measurement of the Secondary Cosmic Microwave Background Anisotropies from the SPT-SZ + SPTpol Surveys

C. L. Reichardt^{1,2} , S. Patil¹ , P. A. R. Ade³ , A. J. Anderson⁴, J. E. Austermann^{5,6}, J. S. Avva⁷, E. Baxter^{8,9} , J. A. Beall⁵, A. N. Bender^{10,11}, B. A. Benson^{4,11,12} , F. Bianchini¹ , L. E. Bleem^{10,11} , J. E. Carlstrom^{10,11,12,13,14}, C. L. Chang^{10,11,12}, P. Chabab¹, H. C. Chiang^{15,16}, T. L. Chou¹³, R. Citron¹⁷ , C. Corbett Moran¹⁸, T. M. Crawford^{11,12} , A. T. Crites^{11,12,19}, T. de Haan^{7,20}, M. A. Dobbs^{15,21} , W. Everett²² , J. Gallicchio^{11,23}, E. M. George^{7,24} , A. Gilbert¹⁵, N. Gupta¹ , N. W. Halverson^{6,22}, N. Harrington⁷, J. W. Henning^{10,11}, G. C. Hilton⁵, G. P. Holder^{21,25,26} , W. L. Holzapfel⁷, J. D. Hrubes¹⁷, N. Huang⁷, J. Hubmayr⁵, K. D. Irwin^{27,28}, L. Knox²⁹, A. T. Lee^{7,20} , D. Li^{5,27}, A. Lowitz¹², D. Luong-Van¹⁷, J. J. McMahon³⁰, J. Mehl^{11,12}, S. S. Meyer^{11,12,13,14} , M. Millea²⁹, L. M. Mocuano^{11,12} , J. J. Mohr^{31,32}, J. Montgomery¹⁵, A. Nadolski^{25,26}, T. Natoli^{11,12,33}, J. P. Nibarger⁵, G. Noble¹⁵, V. Novosad³⁴, Y. Omori^{28,35}, S. Padin^{11,12,19}, C. Pryke³⁶, J. E. Ruhl³⁷, B. R. Saliwanchik^{37,38} , J. T. Sayre^{6,22,37}, K. K. Schaffer^{11,14,39}, E. Shirokoff¹¹, C. Sievers¹⁷, G. Smecher^{15,40} , H. G. Spieler²⁰, Z. Staniszewski³⁷, A. A. Stark⁴¹ , C. Tucker³, K. Vanderlinde^{33,42} , T. Veach⁴³, J. D. Vieira^{25,26} , G. Wang¹⁰, N. Whitehorn⁴⁴ , R. Williamson^{12,17}, W. L. K. Wu¹¹ , and V. Yefremenko¹⁰

¹ School of Physics, University of Melbourne, Parkville, VIC 3010, Australia; christian.reichardt@unimelb.edu.au

² ARC Centre of Excellence for All Sky Astrophysics in 3 Dimensions (ASTRO 3D), Australia

³ Cardiff University, Cardiff CF10 3XQ, UK

⁴ Fermi National Accelerator Laboratory, MS209, P.O. Box 500, Batavia, IL 60510, USA

⁵ NIST Quantum Devices Group, 325 Broadway Mailcode 817.03, Boulder, CO 80305, USA

⁶ Department of Physics, University of Colorado, Boulder, CO 80309, USA

⁷ Department of Physics, University of California, Berkeley, CA 94720, USA

⁸ Institute for Astronomy, University of Hawai'i, 2680 Woodlawn Drive, Honolulu, HI 96822, USA

⁹ Department of Physics and Astronomy, University of Pennsylvania, Philadelphia, PA 19104, USA

¹⁰ High Energy Physics Division, Argonne National Laboratory, 9700 S. Cass Avenue, Argonne, IL 60439, USA

¹¹ Kavli Institute for Cosmological Physics, University of Chicago, 5640 South Ellis Avenue, Chicago, IL 60637, USA

¹² Department of Astronomy and Astrophysics, University of Chicago, 5640 South Ellis Avenue, Chicago, IL 60637, USA

¹³ Department of Physics, University of Chicago, 5640 South Ellis Avenue, Chicago, IL 60637, USA

¹⁴ Enrico Fermi Institute, University of Chicago, 5640 South Ellis Avenue, Chicago, IL 60637, USA

¹⁵ Department of Physics, McGill University, 3600 Rue University, Montreal, QC H3A 2T8, Canada

¹⁶ School of Mathematics, Statistics & Computer Science, University of KwaZulu-Natal, Durban, South Africa

¹⁷ University of Chicago, 5640 South Ellis Avenue, Chicago, IL 60637, USA

¹⁸ Jet Propulsion Laboratory, 4800 Oak Grove Drive, Pasadena, CA 91109, USA

¹⁹ California Institute of Technology, MS 249-17, 1216 E. California Blvd., Pasadena, CA 91125, USA

²⁰ Physics Division, Lawrence Berkeley National Laboratory, Berkeley, CA 94720, USA

²¹ Canadian Institute for Advanced Research, CIFAR Program in Gravity and the Extreme Universe, Toronto, ON M5G 1Z8, Canada

²² Department of Astrophysical and Planetary Sciences, University of Colorado, Boulder, CO 80309, USA

²³ Harvey Mudd College, 301 Platt Blvd., Claremont, CA 91711, USA

²⁴ European Southern Observatory, Karl-Schwarzschild-Str. 2, D-85748 Garching bei München, Germany

²⁵ Astronomy Department, University of Illinois at Urbana-Champaign, 1002 W. Green Street, Urbana, IL 61801, USA

²⁶ Department of Physics, University of Illinois Urbana-Champaign, 1110 W. Green Street, Urbana, IL 61801, USA

²⁷ SLAC National Accelerator Laboratory, 2575 Sand Hill Road, Menlo Park, CA 94025, USA

²⁸ Dept. of Physics, Stanford University, 382 Via Pueblo Mall, Stanford, CA 94305, USA

²⁹ Department of Physics, University of California, One Shields Avenue, Davis, CA 95616, USA

³⁰ Department of Physics, University of Michigan, 450 Church Street, Ann Arbor, MI 48109, USA

³¹ Max-Planck-Institut für extraterrestrische Physik, Giessenbachstr. D-85748 Garching, Germany

³² Excellence Cluster Universe, Boltzmannstr. 2, D-85748 Garching, Germany

³³ Dunlap Institute for Astronomy & Astrophysics, University of Toronto, 50 St George St., Toronto, ON M5S 3H4, Canada

³⁴ Materials Sciences Division, Argonne National Laboratory, 9700 S. Cass Avenue, Argonne, IL 60439, USA

³⁵ Kavli Institute for Particle Astrophysics and Cosmology, Stanford University, 452 Lomita Mall, Stanford, CA 94305, USA

³⁶ School of Physics and Astronomy, University of Minnesota, 116 Church Street SE Minneapolis, MN 55455, USA

³⁷ Physics Department, Center for Education and Research in Cosmology and Astrophysics, Case Western Reserve University, Cleveland, OH 44106, USA

³⁸ Department of Physics, Yale University, P.O. Box 208120, New Haven, CT 06520-8120, USA

³⁹ Liberal Arts Department, School of the Art Institute of Chicago, 112 S. Michigan Ave., Chicago, IL 60603, USA

⁴⁰ Three-Speed Logic, Inc., Victoria, BC V8S 3Z5, Canada

⁴¹ Center for Astrophysics, Harvard & Smithsonian, 60 Garden Street, Cambridge, MA 02138, USA

⁴² Department of Astronomy & Astrophysics, University of Toronto, 50 St George St., Toronto, ON M5S 3H4, Canada

⁴³ Department of Astronomy, University of Maryland College Park, MD 20742, USA

⁴⁴ Department of Physics and Astronomy, University of California, Los Angeles, CA 90095, USA

Received 2020 February 13; revised 2020 November 6; accepted 2020 December 14; published 2021 February 24

Abstract

We report new measurements of millimeter-wave power spectra in the angular multipole range $2000 \leq \ell \leq 11,000$ (angular scales $5' \gtrsim \theta \gtrsim 1'$). By adding 95 and 150 GHz data from the low-noise 500 deg² SPTpol survey to the SPT-SZ three-frequency 2540 deg² survey, we substantially reduce the uncertainties in these bands. These power spectra include contributions from the primary cosmic microwave background, cosmic infrared background, radio galaxies, and thermal and kinematic Sunyaev–Zel’dovich (SZ) effects. The data favor a thermal SZ (tSZ) power at 143 GHz of $D_{3000}^{\text{tSZ}} = 3.42 \pm 0.54 \mu\text{K}^2$ and a kinematic SZ (kSZ) power of $D_{3000}^{\text{kSZ}} = 3.0 \pm 1.0 \mu\text{K}^2$. This is the

first measurement of kSZ power at $\geq 3\sigma$. However, different assumptions about the CIB or SZ models can reduce the significance down to 2.4σ in the worst case. We study the implications of the measured kSZ power for the epoch of reionization under the Calabrese et al. model for the kSZ power spectrum and find the duration of reionization to be $\Delta z_{\text{re}} = 1.1_{-0.7}^{+1.6}$ ($\Delta z_{\text{re}} < 4.1$ at 95% confidence), when combined with our previously published tSZ bispectrum measurement. The upper limit tightens to $\Delta z_{\text{re}} < 3.2$ if the assumed homogeneous kSZ power is increased by 25% ($\sim 0.5 \mu\text{K}^2$) and relaxes to $\Delta z_{\text{re}} < 5.2$ if the homogeneous kSZ power is decreased by the same amount.

Unified Astronomy Thesaurus concepts: [Sunyaev-Zeldovich effect \(1654\)](#); [Cosmic microwave background radiation \(322\)](#); [Reionization \(1383\)](#)

1. Introduction

The cosmic microwave background (CMB) is best known for providing a snapshot of the early universe. However, on small angular scales, secondary anisotropies in the CMB, created by interactions between CMB photons and large-scale structure, also provide clues about the late-time universe. In particular, these secondary anisotropies encode information about the amplitude of structure growth and duration of the epoch of reionization (EoR).

The most significant secondary anisotropies at angular scales of a few arcminutes are the kinematic and thermal Sunyaev-Zel’dovich (SZ) effects. Both SZ effects are due to CMB photons scattering off of free electrons along their path. The kinematic SZ (kSZ) effect is due to an induced Doppler shift in the scattered photons, and thus the kSZ signal from a given volume element is proportional to $(v/c)n_e$, where v is the bulk velocity of the electrons and n_e is the number density of free electrons. The kSZ power spectrum is expected to have significant contributions from the EoR owing to the large contrasts in ionization fraction as the universe reionizes (Gruzinov & Hu 1998; Knox et al. 1998), and at late times when there are larger relative velocities and density contrasts (e.g., Shaw et al. 2012; Battaglia et al. 2013a).

In contrast, the thermal SZ (tSZ) effect is due to the energy transfer from hot electrons to the colder CMB photons and has a signal amplitude of $(k_B T_e/m_e c^2)n_e$, where m_e is the mass of the electron and T_e is the temperature of the electrons. While the kSZ effect does not change the CMB spectrum, the net energy transfer to the photons in the tSZ effect translates to a reduction in the number of CMB photons below 217 GHz as these photons are upscattered toward higher frequencies. One can use the difference in how the tSZ and kSZ effects scale with frequency to simultaneously measure both terms. The tSZ anisotropy signal scales steeply with the normalization of the matter power spectrum, which can be parameterized by σ_8 , the rms of the $z=0$ linear mass distribution on $8h^{-1}$ Mpc scales (e.g., Komatsu & Seljak 2002).

The secondary CMB anisotropies are not the only sources of anisotropy in millimeter-wave maps on arcminute scales. Galaxies also emit at these wavelengths, both synchrotron-dominated active galactic nuclei (AGNs; e.g., De Zotti et al. 2010) and thermal dust emission from dusty star-forming galaxies (DSFGs; e.g., Planck Collaboration et al. 2011; Mocanu et al. 2013; Everett et al. 2020). While the brightest of these sources can be individually detected and masked, it is impossible to remove all of the fainter galaxies, as there are many such DSFGs within each square arcminute (Lagache et al. 2005; Casey et al. 2014). The DSFG signal can be split between a term that does not spatially cluster (the ‘‘Poisson’’ component) and a spatially clustered term (Viero et al. 2013)

We can separate the AGNs and DSFGs from the SZ effects using both angular and spectral information.

1.1. Previous Measurements

Measurements of the millimeter sky at arcminute scales have been made by both the Atacama Cosmology Telescope (ACT; Das et al. 2011, 2014) and South Pole Telescope (SPT) SZ survey (Lueker et al. 2010; Shirokoff et al. 2011; Reichardt et al. 2012; George et al. 2015). The ACT collaboration (Dunkley et al. 2013; Das et al. 2014) measured $D_{3000}^{\text{tSZ}} = 3.3 \pm 1.4 \mu\text{K}^2$ and $D_{3000}^{\text{kSZ}} < 8.6 \mu\text{K}^2$ (95% CL) at 150 GHz and $\ell = 3000$. The final SPT-SZ bandpowers reported by George et al. (2015, hereafter G15) led to even tighter constraints on the tSZ power at 143 GHz of $D_{3000}^{\text{tSZ}} = 4.08_{-0.67}^{+0.58} \mu\text{K}^2$ and on the kSZ power of $D_{3000}^{\text{kSZ}} = 2.9 \pm 1.3 \mu\text{K}^2$. On larger scales, $\ell \leq 2000$, the Planck collaboration made a high-significance detection of the tSZ power spectrum (Planck Collaboration et al. 2014, 2016).

The data used to constrain the tSZ and kSZ power spectra can also teach us about the cosmic infrared background (CIB), radio galaxies, and the correlation between the CIB and galaxy clusters. G15 detected a nonzero correlation between the CIB and galaxy clusters, modeled as a constant, at a significance of more than 3σ , finding $\xi = 0.113_{-0.054}^{+0.057}$.

1.2. This Work

This work adds data from the low-noise 500 deg² SPTpol survey to the 2540 deg² SPT-SZ survey maps used by G15. The SPTpol data substantially reduce the map noise at 95 and 150 GHz over the 500 deg² that was observed by both surveys; however, the 220 GHz maps are unchanged from G15 since SPTpol did not observe at 220 GHz. The lower noise levels at 95 GHz yield a threefold reduction in the bandpower uncertainties at 95×95 GHz; the improvement is more modest ($\sim 30\%$) but still significant at 150×150 GHz.

The outline of this work is as follows. We review the observations and power spectrum analysis in Section 2. Systematics checks done on the data are described in Section 3, before the bandpowers are presented in Section 4. We discuss the modeling of the bandpowers in Section 5 and the constraints on this model in Section 6. We explore the implications for the EoR in Section 7 before concluding in Section 8.

2. Data and Analysis

We present power spectra from the combined SPT-SZ and SPTpol surveys at 95, 150, and 220 GHz. We use a pseudo- C_ℓ cross-spectrum method (Hivon et al. 2002; Polenta et al. 2005;

Tristram et al. (2005) to estimate the power spectra. The data are calibrated by comparing to the Planck 2015 CMB maps.

2.1. Data

This work uses data from the SPT-SZ and SPTpol cameras on the South Pole Telescope. Details on the telescope and cameras can be found in Ruhl et al. (2004), Padin et al. (2008), Shirokoff et al. (2009), Carlstrom et al. (2011), Henning et al. (2012), Sayre et al. (2012), and Austermann et al. (2012).

As described by G15, the 2540 deg² SPT-SZ survey was conducted from 2008 to 2011. The survey region was split into 19 contiguous subpatches, referred to as fields, for observations. The specific field locations and extents can be found in Table 1 of Story et al. (2013, hereafter S13). The SPTpol 500 deg² survey fully or partially overlaps 6 of these 19 fields. Bandpowers for the 13 non-overlapping fields are identical to G15 (except for an updated calibration; see Section 2.2).

We treat the overlapping region as a single field and co-add the time-ordered data (TOD) from both SPTpol and SPT-SZ data into maps. Details of the TOD, filtering, and mapmaking can be found in Shirokoff et al. (2011) for the SPT-SZ data and in Henning et al. (2018) for the SPTpol data. The SPTpol filtering options have been tuned to closely match the SPT-SZ maps used by G15. After combining data from the full 2540 deg², the approximate statistical weight from the new SPTpol data in the combined bandpowers is 83% at 95 GHz, 44% at 150 GHz, and 0% at 220 GHz.

2.2. Beams and Calibration

The SPT-SZ beams are measured using a combination of bright point sources in each field, Venus, and Jupiter as described in Shirokoff et al. (2011). The SPTpol beams are measured using Venus alone as described by Henning et al. (2018). We take a weighted average, based on the statistical weight of each data set in the map, of the beams from the two experiments to estimate the effective beam of the combined survey. Note that the final bandpowers should be robust to an error in this effective beam calculation since the transfer function simulations (Section 2.3.2) use the correct beams for each period of data. For both experiments, the main lobes of the beam are well represented by 1'7, 1'2, and 1'0 FWHM Gaussians at 95, 150, and 220 GHz, respectively.

We use the absolute calibration factors calculated by Hou et al. (2018) and Mocanu et al. (2019) for the SPT-SZ data and the absolute calibration from Henning et al. (2018) for the SPTpol data. In both cases, the calibration is determined by comparing the SPT-SZ (or SPTpol) maps with Planck maps in the same region of sky. The uncertainties are correlated between frequency bands owing to sample variance. The final uncertainties in power are [0.33%, 0.18%, 0.42%] at [95, 150, 220] GHz.

The treatment of the beam and calibration uncertainties in the parameter estimation is described in Section 2.3.5.

2.3. Power Spectrum Estimation

Following G15, we use a pseudo- C_ℓ method to estimate the power spectrum (Hivon et al. 2002). Pseudo- C_ℓ methods start by calculating a (biased) power spectrum from the Fourier transform of the map (in flat sky) and then correct this biased spectrum for effects such as TOD filtering, beams, and finite sky coverage (Hivon et al. 2002). Following Polenta et al.

(2005) and Tristram et al. (2005), we use cross-spectra instead of auto-spectra to avoid noise bias in the result. We report the power spectrum in terms of \mathcal{D}_ℓ , where

$$\mathcal{D}_\ell = \frac{\ell(\ell + 1)}{2\pi} C_\ell. \quad (1)$$

More details on the power spectrum estimator can be found in previous SPT-SZ papers (e.g., Lueker et al. 2010; Reichardt et al. 2012, hereafter R12; G15). We emphasize that for the 13 non-overlapping fields, this work simply reuses the G15 bandpowers for each field. We briefly describe the method in the following sections, focusing on the part that is new in this work—the power spectrum estimation for the combined SPT-SZ + SPTpol maps.

2.3.1. Cross-spectra

Before Fourier-transforming the maps, we apply a window to each map that smoothly goes to zero at the map edges. The window also masks point sources above 6.4 mJy at 150 GHz from the source catalog in Everett et al. (2020). The mask for each point source has a $2'$ -radius disk for sources detected with $S_{150 \text{ GHz}} \in [6.4, 50]$ mJy and a $5'$ -radius disk for sources above 50 mJy. In both cases, a Gaussian taper with $\sigma_{\text{taper}} = 5'$ is applied outside the radius of the disk. For the combined SPTpol and SPT-SZ field that has anisotropic noise due to variations in the amount of integration time, this window also preferentially weights the lower noise regions.

After Fourier-transforming the windowed maps, we take the weighted average of the two-dimensional power spectrum within an ℓ -bin b ,

$$\widehat{D}_b^{\nu_i \times \nu_j AB} \equiv \left\langle \frac{\ell(\ell + 1)}{2\pi} \text{Re} [\tilde{m}_\ell^{\nu_i A} \tilde{m}_\ell^{\nu_j B*}] \right\rangle_{\ell \in b}, \quad (2)$$

where $\tilde{m}^{\nu_i A}$ is the Fourier-transformed map. Here A, B are the observation indices, while ν_i, ν_j are the observation frequencies (e.g., 150 GHz). We average all cross-spectra \widehat{D}_b^{AB} that have $A \neq B$ to get the binned power spectrum \widehat{D}_b . As in R12, we eliminate the noisier modes along the scan direction by excluding modes with $\ell_x < 1200$. We refer to the binned power, \widehat{D}_b , as a “bandpower.”

2.3.2. Simulations

The transfer function and sample variance for the combined SPTpol and SPT-SZ field are calculated from a suite of 200 signal-only simulations. We convolve the simulated skies by the measured beam for each frequency and observing year before sampling the realizations based on the pointing information. The simulated TOD are filtered and binned into maps in the same way as the real data.

The simulated skies include Gaussian realizations of the best-fit lensed Planck 2013 Λ CDM primary CMB model, SZ models, and extragalactic source contributions. Following G15, the kSZ power spectrum is based on the Sehgal et al. (2010) simulations with an amplitude of $2.0 \mu\text{K}^2$ at $\ell = 3000$. The tSZ power spectrum is taken from the Shaw et al. (2010) simulations, normalized to have an amplitude of $4.4 \mu\text{K}^2$ at $\ell = 3000$ at 153 GHz. The extragalactic source term can be split into three components: spatially clustered and Poisson-distributed DSFGs, and Poisson-distributed radio galaxies. Motivated by the predictions of the De Zotti et al. (2005) model

for a 6.4 mJy flux cut at 150 GHz, the radio power is set to $D_{3000}^r = 1.28 \mu\text{K}^2$ at 150 GHz. We assume a radio spectral index of $\alpha_r = -0.53^{45}$ and 1σ scatter on the spectral index of 0.1. The DSFG Poisson power is set to $7.54 \mu\text{K}^2$ at 154 GHz with a modified blackbody spectrum⁴⁶ with $T_{\text{dust}} = 12$ K and $\beta = 2$. The clustered DSFG component is modeled by a $D_\ell \propto \ell^{0.8}$ term normalized to $D_{3000}^c = 6.25 \mu\text{K}^2$ and the same spectral dependence as the Poisson DSFG. Each of the frequency-dependent terms (tSZ, radio, CIB) is estimated at the effective frequency for the nominal band noted in Section 5.1, e.g., 96.9 GHz for the 95 GHz band CIB map. These simulations do not include non-Gaussianity in the tSZ, kSZ, and extragalactic source signals and therefore slightly underestimate the sample variance on these terms. While this would increase the uncertainties on these terms in Section 6, the effect is very minor. In particular, the non-Gaussian variance of the tSZ term on this survey size is $<10\%$ (Millea et al. 2012), which is small compared to the 30% model uncertainty assumed when interpreting the tSZ power. We also estimate the non-Gaussian variance of the kSZ term on a 2500 deg^2 survey using the Flender (ModI) kSZ map (Flender et al. 2016), finding the power level to vary by 2.3%. This variance is very small compared to the kSZ measurement uncertainties in Section 6.

2.3.3. Covariance Estimation and Conditioning

In order to compare the measured bandpowers to theory, we need to estimate a covariance matrix including both sample variance and instrumental noise variance. As in R12 and G15, the sample variance is estimated from signal-only simulations (Section 2.3.2), and the noise variance is empirically determined from the distribution of the cross-spectrum bandpowers $D_b^{\nu_i \times \nu_j, AB}$ between observations A and B and frequencies ν_i and ν_j . A noisy estimate of the bandpower covariance matrix could degrade parameter constraints (see, e.g., Dodelson & Schneider 2013). Thus, we follow G15 and “condition” the covariance matrix to minimize the noise on the covariance estimate and largely avoid this degradation.

The covariance matrix depends on the signal power and, if both bandpowers share a common map, the noise power. As the errors on the off-diagonal elements include terms proportional to the (potentially much larger) diagonal elements, the uncertainty on the off-diagonal elements can be large compared to the true covariance. As a result, we estimate these values analytically from the diagonal elements using the equations in Appendix A of L10.

2.3.4. Field Weighting

We follow G15 and weight each field and frequency cross-spectrum based on the average of the inverse of the diagonal of the covariance matrix over the bins $2500 < \ell < 3500$. These weights adjust for the differences in noise and sample variance between fields; beam and calibration errors are deliberately not included. As argued by G15, the angular range, $2500 < \ell < 3500$, is where the data have the most sensitivity to SZ signals.

⁴⁵ That is, the radio source flux in Jy is proportional to ν^{α_r} , where ν is the frequency.

⁴⁶ That is, the dusty galaxy flux in Jy is proportional to $\nu^\beta B_\nu(T_{\text{dust}})$.

We calculate the combined bandpowers, D_b , as

$$D_b = \sum_i D_b^i w_i, \quad (3)$$

where D_b^i is the bandpower of field i and w_i is the weight. The covariance matrix likewise can be expressed as

$$C_{bb'} = \sum_i w_i C_{bb'}^i w_i. \quad (4)$$

The sum of the weights is normalized to unity.

2.3.5. Beam and Calibration Uncertainties

To handle the calibration uncertainties, we include three calibration factors in the parameter fitting, one per frequency. We marginalize over these three factors, with a prior based on the measured calibration uncertainty for all parameter fits.

We follow Aylor et al. (2017) for the treatment of beam uncertainties. The beam correlation matrix, $\rho_{bb'}^{\text{beam}}$, is calculated as described by G15, using the fractional beam errors for each year and the relative weights of each year of data over the SPT-SZ and SPTpol surveys. At each step in the chain, we use the predicted theory bandpowers (D_b^{theory}) to convert this beam correlation matrix into a beam covariance according to

$$C_{bb'}^{\text{beam}} = \rho_{bb'}^{\text{beam}} D_b^{\text{theory}} D_{b'}^{\text{theory}}. \quad (5)$$

We add this beam covariance to the bandpower covariance matrix that contains the effects of sample variance and instrumental noise. The likelihood for that specific theoretical model is then evaluated using this combined covariance matrix.

3. Null Tests

We test the data for unknown systematic errors by running two null tests. A null test consists of dividing the set of maps into two halves. The power spectrum of the difference between the maps of these two halves should be consistent with zero since all true astrophysical signals are canceled out. In practice, there can be slight amounts of residual power due to, for instance, small pointing differences. We calculate the expectation for the tiny amount of remaining power by applying the same differencing process to simulations. Detecting a significant deviation from this expectation would signal the presence of a systematic error. Note that we only run new null tests for the combined SPT-SZ and SPTpol field; we do not rerun null tests for the fields that have been reused from G15. We look at the following data splits for systematic effects:

1. Scan direction: We subtract left-going from right-going scans to test for potential systematics related to the telescope’s motion. This test is also sensitive to incorrect detector time constants.
2. Time: We split the data based on when they were observed. We subtract data from the first half of the observations of a field from data from the second half. Note that we split the data such that half 1 had the first half of the SPT-SZ observations plus the first half of the SPTpol observations, rather than all of the SPT-SZ observations plus some SPTpol observations. The null tests demonstrate the long-term temporal stability of the instruments. For instance, a slow drift in calibration would cause the test to fail.

We find one failure in the null tests. The first-half-minus-second-half null test at 150 GHz shows excess power at $\ell < 2500$. While this excess is statistically significant (approximately 4σ in two bins), it is also extremely small, $< 0.1\%$ of the non-nulled power at these scales. The failure could be partially explained by drift in the relative calibration over time (this reduces the excess χ^2 from ~ 30 to ~ 9). Such a drift would not significantly affect the final power spectrum, as the absolute calibration procedure ties the full co-add map to the Planck map on the same area of sky. The failure might also be related to a temporal variation in ground pickup. Given the small amount of power, relative to either the bandpowers or the sample variance in these bins, we choose to proceed with the analysis.

4. Bandpowers

We apply the analysis of Section 2.3 to the co-added SPTpol and SPT-SZ maps. Masking point sources above 6.4 mJy at 150 GHz leads to a final effective area of 464 deg² for the combined SPTpol plus SPT-SZ field. We combine the resulting bandpowers with those from the other 13 fields in G15 according to Section 2.3.4. As in G15, we measure the power spectra across the range of $2000 < \ell < 11,000$. Following G15, we restrict the 95×95 GHz bandpowers to $\ell < 8800$ owing to the larger beam size at 95 GHz. The new bandpowers are listed in Table 1 and plotted in Figure 1. The bandpowers, covariance matrix, and window functions are available for download on the SPT⁴⁷ and LAMBDA⁴⁸ websites.

The observed power is dominated by the primary CMB anisotropy on large angular scales ($\ell < 3500$). On smaller scales, extragalactic sources become important, DSFGs at 150 and 220 GHz and radio galaxies at 95 GHz. We also see evidence for power from the kinematic and thermal SZ effects. We plot the best-fit model components against the bandpowers at the six frequency combinations in Figure 2.

5. Cosmological Modeling

We fit the SPTpol + SPT-SZ bandpowers to a combination of the primary CMB anisotropy, thermal and kinematic SZ effects, radio galaxies, and DSFGs. The model is described in detail in the Appendix of G15; we only outline it here. The CMB is the most significant term on large angular scales in all bands. On smaller angular scales, the DSFGs contribute the most power at 150 and 220 GHz, while radio galaxies are more significant at 95 GHz. The SZ effects and correlations between the thermal SZ signal and CIB are also included. Finally, although the Galactic cirrus power in these fields and frequency bands is expected to be small, we include Galactic cirrus in our modeling, with an external prior on the amplitude and shape.

We use the 2019 October version of CosmoMC⁴⁹ (Lewis & Bridle 2002) to calculate parameter constraints. We have added code to model the foregrounds and secondary anisotropies, which is based on the code used by G15. The source code and instructions to compile are available on the SPT website (see footnote 47).

Unless otherwise noted, we fix the six Λ CDM parameters to the best-fit values. The best-fit values are taken from a combined likelihood with the Planck 2018 TT, TE, and EE data

and the bandpowers of this work. We find that allowing the Λ CDM parameters to vary does not noticeably affect the recovered posteriors for the foreground and secondary anisotropy parameters, and the Markov Chain Monte Carlo steps are much faster with the Λ CDM parameters fixed.

The cirrus model and strong prior on its amplitude are the same as in G15. We have tested removing this prior and have found negligible shifts ($< 0.2\sigma$) in other parameters.

Two terms in the modeling describe the kSZ and tSZ power spectra. We model the tSZ power as a free amplitude (defined by the power at $\ell = 3000$ and 143 GHz) that scales the Shaw et al. (2010) tSZ model template. We assume the nonrelativistic tSZ frequency scaling. In Section 6.1.3, we also check whether the results depend on the template chosen. Similarly, we describe the kSZ power by an amplitude parameter (defined by the power at $\ell = 3000$) that scales a template constructed by setting the power of the CSF⁵⁰ homogeneous kSZ template from Shaw et al. (2012) and patchy kSZ template from Zahn et al. (2012, hereafter Z12) to be equal at $\ell = 3000$. Slightly differently than the tSZ case, we test the data's sensitivity to the exact angular dependence of the kSZ power in Section 6.1.3 by simultaneously fitting separate amplitudes for the homogeneous and patchy kSZ terms.

We include two parameters to describe the radio Poisson power: the amplitude of the radio Poisson power at 150 GHz and $\ell = 3000$, and the spectral index α_{rg} for the radio galaxies. Unlike in G15, we do not place a prior on the radio galaxy power, as the 95 GHz data constrain it well.

In the baseline model, we include five parameters to describe the DSFGs that make up the CIB. Three of these parameters are amplitudes of the Poisson, one-halo clustering, and two-halo clustering power at $\ell = 3000$ and 150 GHz. As in G15, the one- and two-halo clustering templates are taken from the best-fit halo model in Viero et al. (2013). The other two parameters are the graybody indices β for the Poisson and clustering power. We assume that there is no difference in the frequency scaling between the one- and two-halo clustering terms.

Finally, we include the expected anticorrelation between the CIB and tSZ power spectra. An anticorrelation is expected below the peak of the CMB blackbody because a dark matter overdensity will be associated with an overdensity of DSFGs (positive signal) and hot gas (negative tSZ signal). We take the angular dependence of the anticorrelation to be described by the form found by Z12, when looking at the Shang et al. (2012) CIB simulations. However, we allow the magnitude of this anticorrelation to float freely from -1 to 1 , with the magnitude defined at $\ell = 3000$.

Table 2 shows the improvement in the quality of the fits with the sequential introduction of free parameters to the original Λ CDM primary CMB model. There are clear improvements as each parameter is added, up through the kSZ and tSZ-CIB correlation. Changing from a tSZ-CIB correlation that is constant in ℓ to the Z12 form marginally improves the χ^2 by 0.5, without introducing any new parameters. Thus, we include this shape in our baseline model. The other model variations we consider do not significantly improve the quality of the fits. Using a power law for the CIB clustered power, as was done by G15, instead of the simulation-based one- and two-halo terms, is disfavored by the data, with an increase in χ^2 of 2.1 for the same number of parameters.

⁴⁷ <http://pole.uchicago.edu/public/data/reichardt20/>

⁴⁸ http://lambda.gsfc.nasa.gov/product/spt/spt_prod_table.cfm

⁴⁹ <http://cosmologist.info/cosmomc>

⁵⁰ Simulations that included cooling and star formation.

Table 1
Bandpowers

ℓ Range	ℓ_{eff}	95 GHz		150 GHz		220 GHz	
		\hat{D} (μK^2)	σ (μK^2)	\hat{D} (μK^2)	σ (μK^2)	\hat{D} (μK^2)	σ (μK^2)
2001–2200	2077	218.4	3.8	215.6	2.3	286.2	6.5
2201–2500	2332	128.2	1.9	125.9	1.1	201.7	4.3
2501–2800	2636	81.9	1.1	80.29	0.67	170.4	4.1
2801–3100	2940	52.84	0.79	51.88	0.46	156.9	4.0
3101–3500	3293	36.87	0.58	36.89	0.31	155.4	3.7
3501–3900	3696	31.35	0.57	31.19	0.29	182.8	4.4
3901–4400	4148	28.85	0.65	31.24	0.29	202.0	4.8
4401–4900	4651	30.25	0.89	33.62	0.35	245.7	6.0
4901–5500	5203	35.3	1.1	39.73	0.42	290.2	7.0
5501–6200	5855	43.4	1.9	46.34	0.53	349.8	8.7
6201–7000	6607	44.6	3.2	57.24	0.72	435.0	11.0
7001–7800	7408	46.7	6.7	69.5	1.2	524.0	15.0
7801–8800	8310	61.0	12.0	89.0	1.8	665.0	21.0
8801–9800	9311	98.7	2.9	729.0	34.0
9801–11000	10413	122.0	4.5	962.0	49.0

		95 \times 150 GHz		95 \times 220 GHz		150 \times 220 GHz	
2001–2200	2077	213.3	2.9	207.2	4.0	225.9	2.9
2201–2500	2332	123.5	1.4	121.6	2.2	140.7	1.6
2501–2800	2636	76.72	0.82	77.7	1.6	98.8	1.2
2801–3100	2940	47.73	0.54	50.0	1.4	73.03	1.00
3101–3500	3293	32.01	0.36	34.2	1.2	61.78	0.80
3501–3900	3696	24.38	0.34	26.6	1.4	63.77	0.87
3901–4400	4148	22.47	0.35	28.3	1.5	70.62	0.89
4401–4900	4651	22.46	0.46	32.0	2.0	82.4	1.1
4901–5500	5203	25.00	0.58	35.1	2.6	97.1	1.3
5501–6200	5855	28.88	0.79	47.1	3.2	116.6	1.6
6201–7000	6607	34.9	1.2	55.8	5.2	149.8	2.1
7001–7800	7408	39.2	2.0	60.4	8.7	179.1	3.1
7801–8800	8310	45.8	3.3	75.0	13.0	224.0	4.3
8801–9800	9311	74.8	6.5	87.0	29.0	276.1	7.2
9801–11000	10413	83.0	14.0	203.0	62.0	351.0	11.0

Note. Angular multipole range, weighted multipole value ℓ_{eff} , bandpower \hat{D} , and bandpower uncertainty σ for the six auto- and cross-spectra of the 95, 150, and 220 GHz maps with point sources detected at >6.4 mJy at 150 GHz masked at all frequencies. The uncertainties in the table are calculated from the diagonal elements of the covariance matrix, which includes noise and sample variance, but not beam or calibration errors. Due to the larger beam size at 95 GHz, the 95 \times 95 GHz bandpowers are limited to $\ell < 8800$.

5.1. SPT Effective Frequencies

While we refer to the three frequency bands as 95, 150, and 220 GHz for convenience, the actual bandpasses are not simple delta functions. The bandpasses of both SPTpol and SPT-SZ were measured using a Fourier transform spectrometer (FTS). We estimate the calibration uncertainty on the FTS to be 0.3 GHz, which should be coherent between the three bands. Although the uncertainty has negligible effect on the constraints, we marginalize over the FTS calibration uncertainty in all parameter fits for completeness.

With the measured bandpasses in hand, we can calculate an effective band center for each of the potential signals: the thermal SZ effect, the CIB, and synchrotron sources. As we report and calibrate the bandpowers in CMB temperature units, the band center is irrelevant for sources with a CMB-like spectrum. We average the measured band centers for each year using that year’s data relative weight to the final bandpowers. For an $\alpha = -0.5$ (radio-like) source spectrum, we find band centers of 93.5, 149.5, and 215.8 GHz. For an $\alpha = 3.5$ (dust-like) source spectrum, we find band centers of 96.9, 153.4, and 221.6 GHz. For a nonrelativistic tSZ spectrum, we find band centers of 96.6, 152.3, and 220.1 GHz. The ratio of tSZ power

in the 95 GHz band to that in the 150 GHz band is 2.77; the 220 GHz band has nearly zero tSZ power, as it is well matched to the null in the tSZ spectrum near 217 GHz. Note that we quote all tSZ power constraints at 143 GHz, for consistency with Planck, and all other model terms at 150 GHz.

6. Results

6.1. Baseline Model

We begin by presenting results for the baseline model discussed in Section 5. This model includes the best-fit Λ CDM model plus 10 parameters to describe foregrounds. Foreground parameters include the amplitudes of the tSZ power, kSZ power, radio galaxy Poisson power, CIB Poisson power, and CIB one- and two-halo clustered power; two parameters to describe the frequency dependence of the CIB terms; the tSZ-CIB correlation; and the spectral index of radio galaxies. The amplitude of galactic cirrus is allowed to float within a strong prior.

We fit the 88 SPT bandpowers to the model described above. There are 78 degrees of freedom (dof), since the Λ CDM parameters are set to their best-fit values, essentially fixed by

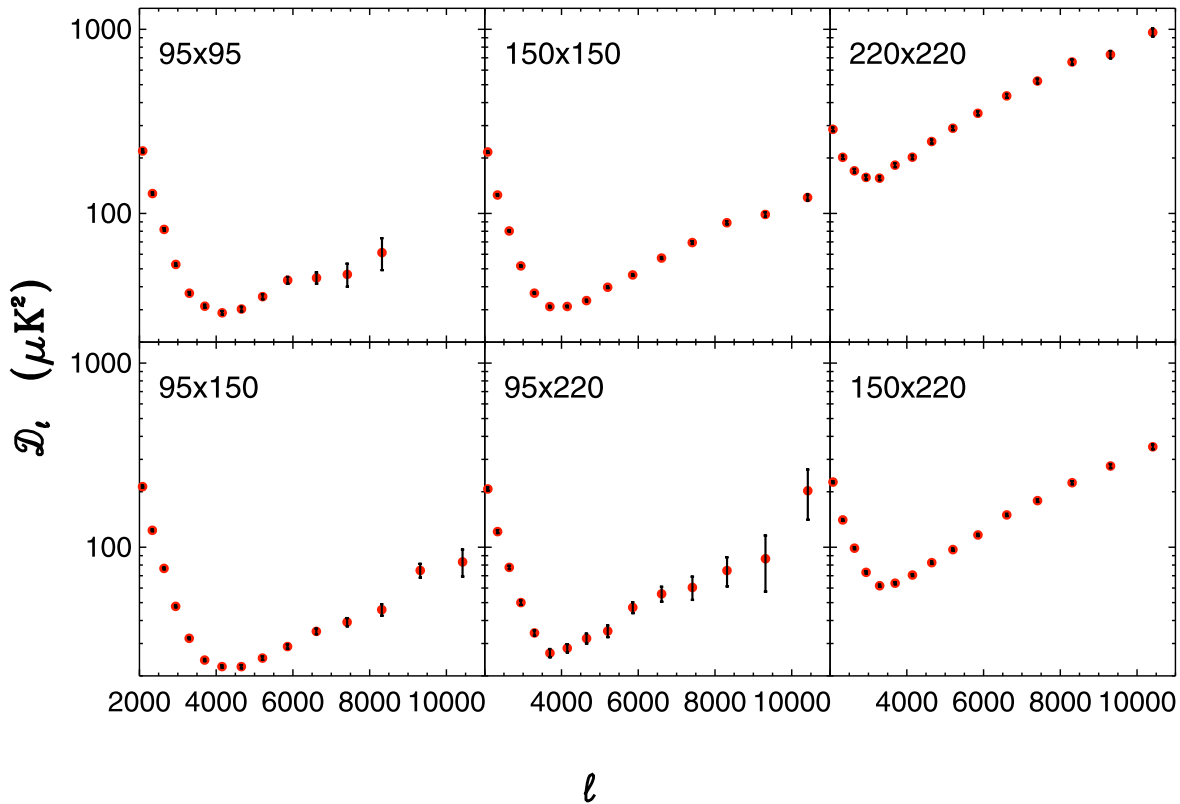


Figure 1. Six auto- and cross-spectra measured with the 95, 150, and 220 GHz SPT data.

the Planck data, leaving the 10 foreground model parameters. Jointly fitting the foreground terms and the Λ CDM parameters with Planck data has little effect on derived foreground constraints. This baseline model fits the SPT data with a $\chi^2 = 99.7$, giving a probability to exceed of 5.0% for our 78 dof, and provides the simplest interpretation of the data.

6.1.1. CIB Constraints

The CIB is detected at very high significance and is especially important at 220 GHz. As highlighted in Table 2, adding the CIB terms to the model improves the fit quality by $\Delta\chi^2 \sim 77,000$. With the flux cut of ~ 6.4 mJy at 150 GHz in this work, the Poisson CIB power is larger than the radio galaxy power by a factor of seven at 150 GHz and by a factor of 60 at 220 GHz. The radio galaxy power is larger than the CIB power at 95 GHz.

At 150 GHz and $\ell = 3000$, we find that the Poisson DSFG component has power $D_{3000}^p = 7.24 \pm 0.63 \mu\text{K}^2$ while the one- and two-halo DSFG clustering terms are $D_{3000}^{1\text{-halo}} = 2.21 \pm 0.88 \mu\text{K}^2$ and $D_{3000}^{2\text{-halo}} = 1.82 \pm 0.31 \mu\text{K}^2$, respectively. At 220 GHz, this scales to $D_{3000}^{p,220\text{ GHz}} = 61.4 \pm 9.0 \mu\text{K}^2$, $D_{3000}^{1\text{-halo},220\text{ GHz}} = 32.4 \pm 11.2 \mu\text{K}^2$, and $D_{3000}^{2\text{-halo},220\text{ GHz}} = 27.5 \pm 4.6 \mu\text{K}^2$. The β in the modified blackbody functional form of $\nu^\beta B_\nu(T)$ rises from 1.48 ± 0.13 for the Poisson term to 2.23 ± 0.18 for the clustered terms. Cast as effective spectral indices from 150 to 220 GHz, these values of β translate to spectral indices of 3.29 ± 0.13 for the Poisson power and 4.04 ± 0.18 for the clustered power. The higher spectral index for the clustered power could indicate a different redshift weighting (the same rest-frame modified blackbody spectrum would appear steeper at low redshift), a dependence

of the galaxy spectral energy distributions on the galaxy mass, or contributions from different source populations, such as are considered to explain the CIB-CXB correlation (e.g., Yue et al. 2013).

The constraints from the baseline model are close to both theoretical expectations and previous work (e.g., Dunkley et al. 2011, G15). When considering a similar foreground model (except for the angular dependence of the tSZ-CIB correlation), G15 found Poisson power levels of $7.59 \pm 0.69 \mu\text{K}^2$ and $63.4 \pm 9.5 \mu\text{K}^2$ at 150 and 220 GHz, respectively. Note that since G15 reported powers at the effective frequency band centers instead of 150 and 220 GHz, to facilitate a comparison we have rescaled the reported numbers to 150 and 220 GHz using the median spectral index in this work. These two sets of constraints agree very closely (0.3σ or 3%–5%). It should be remembered that there is a large overlap between the underlying data, especially at 220 GHz, where only the relative weighting of the data has changed. For the clustered terms, the G15 numbers are $1.6 \pm 0.9 \mu\text{K}^2$ and $1.7 \pm 0.3 \mu\text{K}^2$ for the one- and two-halo terms, respectively. The agreement is still good: the one-halo term has increased by 0.7σ , while the two-halo term dropped by a smaller amount. The same trends continue at 220 GHz: the one-halo term increases by 0.5σ , while the two-halo term falls slightly. We note that the recovered CIB clustering power in G15 was slightly lower than previous measurements. Thus, the shifts here move toward those earlier measurements. The inferred spectral indices of this work are also within 1σ of the values in G15.

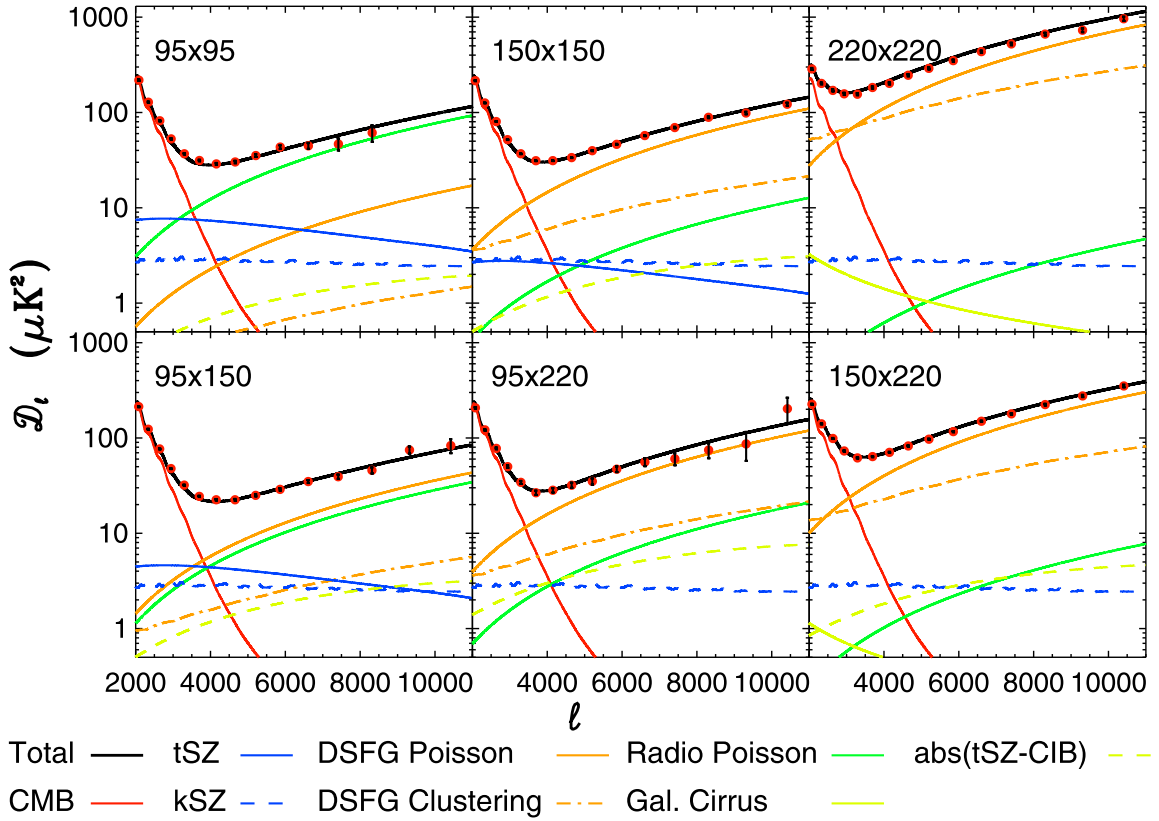


Figure 2. Best-fit baseline model plotted against the SPT 95, 150, and 220 GHz auto- and cross-spectra. We also show the relative power in each component of the model.

6.1.2. Radio Galaxy Constraints

Radio power is detected at high significance at 95 and 150 GHz, with the addition of radio power to the model leading to a large improvement in the fit quality, namely, $\Delta\chi^2 = 5141$ for two parameters. As in G15, the data prefer slightly less radio galaxy power than predicted by the De Zotti et al. (2005) model for a 6.4 mJy flux cut at 150 GHz. The preferred radio power at $\ell = 3000$ is $D_{3000}^{r-150 \times 150} = 1.01 \pm 0.17 \mu\text{K}^2$, about 25% lower than the $1.28 \mu\text{K}^2$ predicted. The population spectral index for the radio power is constrained to be -0.76 ± 0.15 . This is 1σ lower than the median spectral index of -0.60 for synchrotron-classified sources reported by Mocanu et al. (2013). This could be due to random chance, the 150 GHz only selection criteria for masking point sources in this work, or a tendency for the spectral index to flatten for the brightest 150 GHz radio sources, as argued by Mocanu et al. (2013).

6.1.3. SZ Power

As shown in Figure 3, we detect both tSZ and kSZ power. We measure $D_{3000}^{\text{tSZ}} = 3.42 \pm 0.54 \mu\text{K}^2$ and $D_{3000}^{\text{kSZ}} = 3.0 \pm 1.0 \mu\text{K}^2$ for the tSZ and kSZ power, respectively, at $\ell = 3000$ and 143 GHz.

The tSZ (kSZ) power is detected at approximately 7σ (3σ). While our fiducial results assume the Shaw tSZ template (Shaw et al. 2010) and CSF+patchy kSZ template (Z12, Shaw et al. 2012), the current data offer little information about the specific shape of the SZ spectra. The recovered SZ power levels for four different tSZ templates and three kSZ templates are reported in Table 3—no significant shifts are seen between the

different templates considered. The tSZ power spectrum level is a probe of large-scale structure growth and the pressure profiles in galaxy clusters. The total kSZ power has contributions from the EoR and from the bulk flows of large-scale structure at later times; we discuss the implications of the kSZ measurement for reionization in Section 7.

The joint analysis of the SPTpol and SPT-SZ surveys allows the first detection (at 3σ) of kSZ power. The reported kSZ power in this work falls within the 95% CL upper limits on kSZ power reported in previous works (e.g., Dunkley et al. 2013, G15). G15 also report a central value when including a tSZ prior based on the bispectrum of $D_{3000}^{\text{kSZ}} = 2.9 \pm 1.3 \mu\text{K}^2$, which agrees extremely well (although with 30% larger uncertainties) with the value in this work. If we add the same bispectrum-based tSZ prior to the current results, we find $D_{3000}^{\text{kSZ}} = 2.8 \pm 0.9 \mu\text{K}^2$, which translates to a 3.1σ detection of kSZ power.

The joint analysis also significantly reduces the measurement uncertainties on the tSZ power. This tSZ measurement is consistent with ($<1\sigma$) earlier observations of the tSZ power scaled to 143 GHz: $D_{3000}^{\text{tSZ}} = 4.38^{+0.83}_{-1.04} \mu\text{K}^2$ (G15), $D_{3000}^{\text{tSZ}} = 4.20 \pm 1.37 \mu\text{K}^2$ (R12), and $D_{3000}^{\text{tSZ}} = 3.9 \pm 1.7 \mu\text{K}^2$ (Dunkley et al. 2013). With the same bispectrum-based prior, the preferred tSZ power in this work is $D_{3000}^{\text{tSZ}} = 3.53 \pm 0.48 \mu\text{K}^2$.

We also consider the cosmological implication of the measured tSZ power, specifically on σ_8 since the tSZ power scales steeply with σ_8 . We assume the relationship $D_{3000}^{\text{tSZ}} \propto \sigma_8^{8.34}$ (Shaw et al. 2010). We consider three sets of models: the Shaw et al. (2010) model that forecasts a tSZ power at 143 GHz and $\ell = 3000$ of $5.5 \mu\text{K}^2$, the Bhattacharya

Table 2
Delta χ^2 for Model Components

Term	dof	$\Delta\chi^2$
CMB (fixed) + cirrus	...	(reference)
DSFG Poisson	2	-77,175.0
Radio Poisson	2	-5135.0
DSFG clustering	3	-985.0
tSZ	1	-269.0
kSZ + tSZ-CIB Correlation	2	-8.4
ℓ -dependent tSZ-CIB	0	-0.5
<hr/>		
Sloped tSZ-CIB corr.	1	0.0
$T \in [8, 50 \text{ K}]$	2	+0.4
Scatter in spectral indices	2	+0.2
Power law for cluster DSFG	0	+2.1
Separate h- and p-kSZ	1	+0.8

Note. Improvement to the best-fit χ^2 as additional terms are added to the model. Terms above the double line are included in the baseline model, with each row showing the improvement in likelihood relative to the row above it. Note that adding either kSZ or a tSZ-CIB correlation separately leads to a marginal improvement in χ^2 ($\Delta\chi^2 \sim 1-2$), but the improvement is more significant with both parameters included. For rows below the double line, the $\Delta\chi^2$ is shown relative to the baseline model rather than the row above it. None of these extensions significantly improve the fit quality. The row labeled “Sloped tSZ-CIB corr.” multiplies the Shang tSZ-CIB correlation template by a term that varies linearly with ℓ around the pivot point of unity at $\ell = 3000$. The row labeled “ $T \in [8, 50 \text{ K}]$ ” allows the temperature of the modified BB for the Poisson and clustered CIB terms to vary between 8 and 50 K. The row labeled “Scatter in spectral indices” adds two parameters, describing the population variance in spectral indices between CIB and radio galaxies, respectively. The row labeled “Power law for cluster DSFG” replaces the one- and two-halo CIB templates by a power law described by an amplitude and an exponent. While this conserves the total number of model parameters, the power-law form is a worse fit to the data. Finally, in “Separate h- and p-kSZ,” we check whether the data can distinguish between the (small) expected change in angular dependence between the homogeneous and patchy kSZ terms. Surprisingly, allowing two amplitude parameters, one for each kSZ template, results in a worse fit. The uncertainty on all of the quoted $\Delta\chi^2$ values is approximately 0.4.

et al. (2012) model predicting $5.0 \mu\text{K}^2$, and the Battaglia et al. (2012) model predicting $5.9 \pm 0.9 \mu\text{K}^2$ (Dunkley et al. 2013). Ignoring the significant modeling uncertainty, the measured tSZ power favors $\sigma_8 = 0.735 \pm 0.013$, 0.745 ± 0.013 , and 0.730 ± 0.013 , respectively. More fairly allowing for a 30% modeling uncertainty weakens the σ_8 constraints to $\sigma_8 = 0.735 \pm 0.027$, 0.744 ± 0.027 , and 0.730 ± 0.027 , respectively. As noted by G15, the σ_8 levels inferred from the tSZ spectrum are limited by uncertainty in modeling.

The σ_8 value inferred from the observed tSZ power of approximately 0.735 ± 0.027 is consistent at $<1\sigma$ with the $\sigma_8 = 0.763 \pm 0.037$ found by Bocquet et al. (2019) from tSZ-selected galaxy cluster number counts in the SPT-SZ survey. However, as has been noted with earlier cluster results (e.g., Douspis et al. 2019), the σ_8 preferred by the tSZ power spectrum is significantly lower (2.7σ) than the Planck CMB-only result of $\sigma_8 = 0.811 \pm 0.006$ (Planck Collaboration et al. 2018). It remains unclear whether this discrepancy is related to cluster astrophysics or cosmology.

The different CIB models considered in Table 2 have a modest impact on the inferred SZ power levels. For instance, assuming that the tSZ-CIB correlation is independent of angular multipole increases the uncertainties and shifts a small amount of power from the tSZ to kSZ effect. The tSZ power constraint moves from $D_{3000}^{\text{tSZ}} = 3.42 \pm 0.54 \mu\text{K}^2$ to

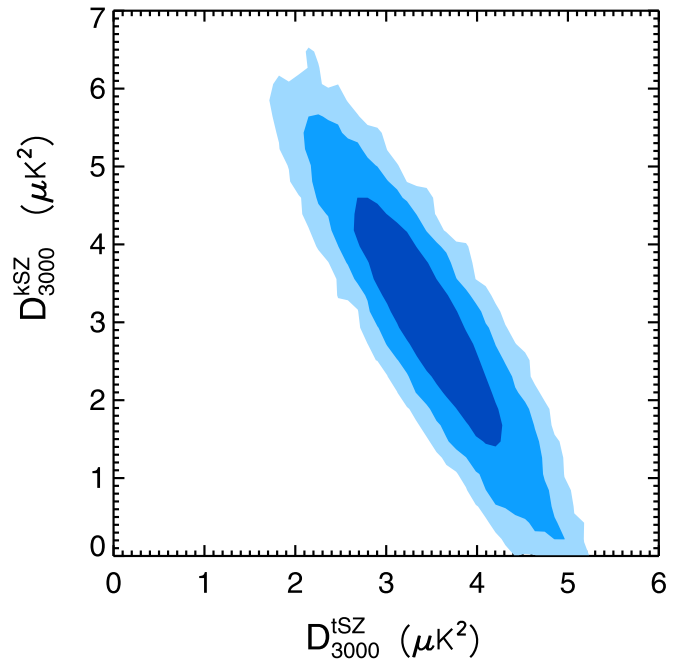


Figure 3. 2D posterior likelihood surface for the tSZ and kSZ power at 143 GHz at $\ell = 3000$ in the baseline model including tSZ-CIB correlations. The 1σ , 2σ , and 3σ constraints are shown in shades of blue. The observed degeneracy is due to the correlation between the tSZ and CIB.

$3.30 \pm 0.64 \mu\text{K}^2$; the kSZ power constraint moves from $D_{3000}^{\text{kSZ}} = 3.0 \pm 1.0 \mu\text{K}^2$ to $3.5 \pm 1.2 \mu\text{K}^2$. Assuming a power law for the clustered CIB model leads to minor shifts: $D_{3000}^{\text{tSZ}} = 3.37 \pm 0.55 \mu\text{K}^2$ and $D_{3000}^{\text{kSZ}} = 3.3 \pm 1.1 \mu\text{K}^2$. Between the CIB models, the tSZ shifts are less than 0.3σ , while the kSZ shifts are less than 0.5σ .

These SZ constraints presume the nonrelativistic tSZ spectrum, which is an imperfect assumption for real galaxy clusters (Remazeilles et al. 2019). We estimate the potential magnitude of this correction by running a chain with the effective tSZ frequencies of each band calculated for a 5 keV tSZ spectrum. We find small shifts in the SZ power level and no change in the CIB terms. For the 5 keV spectrum without the bispectrum prior, the tSZ power increases by 0.5σ to $D_{3000}^{\text{tSZ}} = 3.70 \pm 0.58 \mu\text{K}^2$. There is also a minor increase in the kSZ power by 0.2σ to $3.2 \pm 1.0 \mu\text{K}^2$. The uncertainties on both terms are essentially unchanged. Such small shifts do not substantially change the EoR results in Section 7.2.

6.1.4. tSZ-CIB Correlation

We parameterize the tSZ-CIB correlation with a single parameter ξ that scales the Z12 template for the tSZ-CIB correlation as a function of ℓ . An overdensity of dusty galaxies in galaxy clusters would result in a positive value of ξ . The tSZ-CIB correlation is partially degenerate with the tSZ and kSZ power, as illustrated in Figure 4. Increasing the correlation, ξ , slowly decreases the inferred tSZ power while quickly increasing the inferred kSZ power. We measure the tSZ-CIB correlation to be $\xi = 0.076 \pm 0.040$ at $\ell = 3000$. The data prefer positive tSZ-CIB correlation, ruling out $\xi < 0$ at the 0.983 CL. For easier comparison to past works, we also run a chain with ξ that is constant in ℓ . This does very little to the inferred SZ power levels; the preferred values shift by 0.2σ and 0.3σ for the tSZ and kSZ, respectively. For a constant ξ , the bandpowers in this work favor $D_{3000}^{\text{kSZ}} = 3.5 \pm 1.2 \mu\text{K}^2$ and D_{3000}^{tSZ}

Table 3
SZ Constraints

tSZ Template	kSZ Template	$D_{3000}^{\text{tSZ}} (\mu\text{K}^2)$	$D_{3000}^{\text{kSZ}} (\mu\text{K}^2)$	ξ
Shaw	CSF+patchy	3.42 ± 0.54	3.0 ± 1.0	0.076 ± 0.040
Shaw	CSF	3.39 ± 0.58	3.1 ± 1.3	0.077 ± 0.047
Shaw	Patchy	3.45 ± 0.56	3.5 ± 1.2	0.086 ± 0.050
Battaglia	CSF+patchy	3.74 ± 0.54	2.4 ± 1.0	0.051 ± 0.033
Bhattacharya	CSF+patchy	3.46 ± 0.54	3.0 ± 1.0	0.071 ± 0.036
Sehgal	CSF+patchy	3.59 ± 0.54	2.8 ± 1.0	0.064 ± 0.039
Shaw w. Bispectrum	CSF+patchy	3.53 ± 0.48	2.8 ± 0.9	0.069 ± 0.036

Note. Measured tSZ power, kSZ power, and tSZ-CIB correlation at $\ell = 3000$ (and 143 GHz in the case of the tSZ) for different tSZ and kSZ models. The results are robust to the assumed templates. The first two columns indicate which of three templates has been used for the tSZ and kSZ terms. In the case of the kSZ, the three templates are the CSF homogeneous kSZ template (Shaw et al. 2012), the patchy kSZ template (Z12), or the sum of both. In the case of the tSZ, the three templates are taken from the Battaglia (Battaglia et al. 2013b), Shaw (Shaw et al. 2010), Bhattacharya (Bhattacharya et al. 2012), or Sehgal (Sehgal et al. 2010) simulations. The last row shows the results when a prior on the tSZ power based on the bispectrum measurement by Crawford et al. (2014) is added.

$= 3.30 \pm 0.64 \mu\text{K}^2$. This is somewhat less (1σ) tSZ power than found by G15 in the equivalent case, and slightly more kSZ power (0.4σ). The ξ constraint is $\xi = 0.078 \pm 0.049$. This is well within 1σ of past SPT constraints, $\xi = 0.100_{-0.055}^{+0.069}$ (G15). It is also within the assumed prior range $[0, 0.2]$ of Dunkley et al. (2013).

7. kSZ Interpretation

The most significant improvement in the current study compared to previous works is to the kSZ constraint, with the transition from upper limits to a 3σ detection of power. In this section, we look at what can be learned about the EoR from the kSZ measurement. We do this using the expression for the patchy kSZ power as a function of the timing and duration of reionization (among other cosmological parameters) presented by Calabrese et al. (2014).

7.1. Patchy kSZ Power

To interpret the measured kSZ power in light of the EoR, we must divide up the observed kSZ power between the homogeneous and patchy kSZ signals. As the current data cannot separate the homogeneous kSZ and patchy kSZ power, we consider the inferred patchy kSZ power under three scenarios for the homogeneous kSZ power. The estimate for the homogeneous kSZ power at $\ell = 3000$ is taken from Equation (5) in Calabrese et al. (2014), who in turn base it on the homogeneous kSZ simulations run by Shaw et al. (2012). For the fiducial cosmology in this work, this estimate translates to $D_{3000}^{\text{h-kSZ}} = 1.65 \mu\text{K}^2$. We also include high and low estimates of the homogeneous kSZ power, by rescaling the best guess by factors of 1.25 and 0.75, respectively. For comparison, Shaw et al. (2012) find that a different treatment of helium reionization can scale the homogeneous kSZ signal by ~ 1.22 at $\ell = 3000$.

In all three cases, we take the shape of the homogeneous kSZ power from the CSF model in Shaw et al. (2012). The angular dependence will change slightly for different models, for instance, different helium ionization scenarios change the relative power between $\ell = 3000$ and 10,000 by of order 3%. However, the current data are insensitive to such small shape variations.

With these assumptions about the homogeneous kSZ power in place, we find 95% CL upper limits on the patchy kSZ power of $D_{3000}^{\text{p-kSZ}} < 2.9$ ($3.4/2.5$) μK^2 for the best estimate of the

homogeneous kSZ power (low/high homogeneous kSZ estimates). These limits on the patchy kSZ power are significantly better than the spectra-only limit of $< 4.4 \mu\text{K}^2$ reported by G15, and similar to what was achieved by the addition of the bispectrum prior in G15. If we add the same bispectrum prior to these chains while using the best estimate of the homogeneous kSZ, the patchy kSZ upper limit power reduces by another 10% to $D_{3000}^{\text{p-kSZ}} < 2.5 \mu\text{K}^2$. The 68% confidence interval for the patchy kSZ power with the bispectrum prior is $D_{3000}^{\text{p-kSZ}} = 1.1_{-0.7}^{+1.0} \mu\text{K}^2$.

7.2. Ionization History and the Duration of Reionization

We can transform constraints on the inferred patchy kSZ power, under these assumptions for the homogeneous kSZ power, into constraints on the duration of EoR using the expression for patchy kSZ power in Equation (6) of Calabrese et al. (2014):

$$D_{3000}^{\text{p-kSZ}} = 2.03 \left[\left(\frac{1 + z_{\text{re}}}{11} \right) - 0.12 \right] \left(\frac{\Delta z_{\text{re}}}{1.05} \right)^{0.51} \mu\text{K}^2, \quad (6)$$

which is based on the models of Battaglia et al. (2013b). Here z_{re} is the redshift when the ionization fraction is 50%, and Δz_{re} is the duration of the EoR, defined as the period between 25% and 75% ionization fractions. We also have a choice of prior. For most of this work, results are quoted with a prior that is uniform in power or $D_{3000}^{\text{p-kSZ}}$. However, in an upper limit regime given the relationship between Δz_{re} and $D_{3000}^{\text{p-kSZ}}$, a flat prior on $D_{3000}^{\text{p-kSZ}}$ preferentially favors Δz_{re} near zero. We thus choose to report Δz_{re} constraints under a flat prior on Δz_{re} instead. With these assumptions about the homogeneous kSZ power and this prior on Δz_{re} in place, we find 95% CL upper limits on the duration of the EoR of $\Delta z_{\text{re}} < 5.4$ ($6.9/4.3$) for the best estimate of the homogeneous kSZ power (low/high homogeneous kSZ estimates). With the bispectrum-based prior on the tSZ power added, the limit becomes $\Delta z_{\text{re}} < 4.1$. The 68% confidence interval is $\Delta z_{\text{re}} = 1.1_{-0.7}^{+1.6}$. These limits agree with the recent picture from a variety of observations arguing that reionization happened fairly quickly. Figure 5 shows the likelihoods for Δz_{re} of reionization.

The limits quoted above on the duration of reionization are significantly better than the limits previously set by G15. G15 found an upper limit on the duration of reionization of

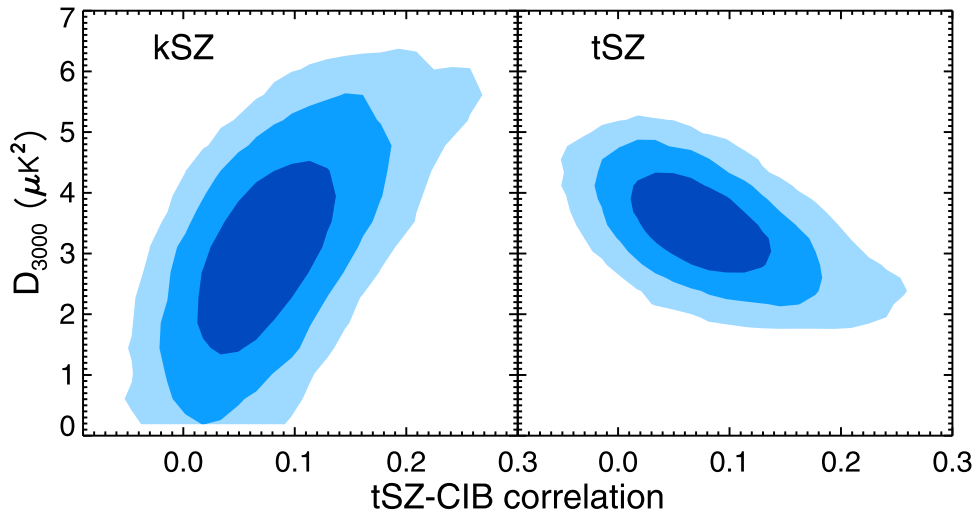


Figure 4. 2D posterior likelihood of the tSZ-CIB correlation and kSZ (left panel) or 143 GHz tSZ power (right panel). The filled contours show the 1σ , 2σ , and 3σ constraints. The data strongly prefer a positive tSZ-CIB correlation, consistent with DSFGs being overdense in galaxy clusters.

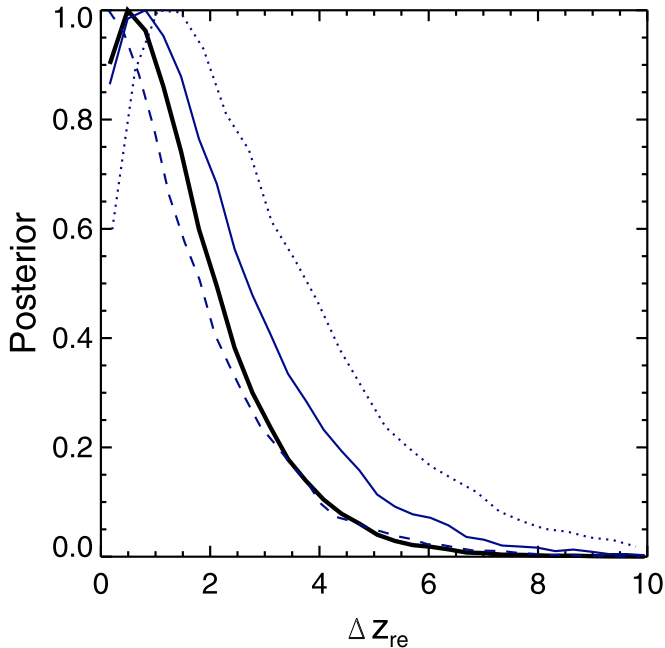


Figure 5. 1D likelihood curves for Δz of reionization with the three assumptions about the homogeneous kSZ power used in this work. The solid blue line is for the expected amount of homogeneous kSZ power, while the dotted and dashed lines reflect the cases where the homogeneous kSZ power is scaled by $\times 0.75$ and 1.25 , respectively. With the best estimate of the homogeneous kSZ power, the 95% CL upper limit on the duration of reionization is $\Delta z < 5.4$. Adding the tSZ bispectrum prior from Crawford et al. (2014) strengthens this limit to $\Delta z_{\text{re}} < 4.1$, as shown by the solid black line.

$\Delta z_{\text{re}} < 5.4$, when including the bispectrum prior. One should be cautious, however, in directly comparing the numbers owing to four model changes. First, G15 defined the duration from 20% to 99% ionization fraction, instead of the 25%–75% in this work. Second, G15 used a higher value for the optical depth from WMAP, which will drive the duration down by roughly a factor of 1.7 for a fixed level of patchy kSZ power. Third, G15 used a uniform prior on the kSZ power instead of a uniform prior on Δz_{re} . Finally, the fiducial homogeneous kSZ model in G15 predicted more power, approximately the high case in this work. Given the degeneracy between the patch and homogeneous kSZ spectra, more homogeneous kSZ power

translates to less patchy kSZ power and a shorter duration. If we reanalyze the G15 bandpowers with the updated calibration, uniform prior in Δz_{re} , Planck optical depth, homogeneous kSZ model, and definition of duration in this work, we find the directly comparable 95% CL upper limit with the bispectrum prior on the duration to be $\Delta z_{\text{re}} < 8.5$. The directly comparable limit with the bispectrum information in this work of $\Delta z_{\text{re}} < 4.1$ is nearly a factor of two lower.

8. Conclusions

We have presented improved measurements of the 95, 150 and 220 GHz auto- and cross-spectra, created by combining data from the 2500 deg² SPT-SZ survey with the low-noise 500 deg² SPTpol survey. The combined data set substantially reduces the bandpower uncertainties over the last SPT release, especially in frequency combinations including 95 GHz data. These bandpowers represent the most sensitive measurements of arcminute-scale anisotropy near the peak of the CMB blackbody spectrum.

The signal at these frequencies and angular scales is composed of the primary CMB temperature anisotropy, DSFGs, radio galaxies, and the kinematic and thermal SZ effects. We fit the data to a 10-parameter model for the DSFGs, radio galaxies, and SZ effects (while fixing the primary CMB power spectrum to the best-fit values). For the first time, we find a 3σ detection of the kSZ power, with a level of $D_{3000}^{\text{kSZ}} = 3.0 \pm 1.0 \mu\text{K}^2$. The observed kSZ power can be deconstructed as the sum of the homogeneous and patchy kSZ terms, which are highly degenerate at current levels of sensitivity. However, using estimates of the homogeneous kSZ power from simulations, we calculate the residual patchy kSZ power and thus limits on the duration of reionization. Assuming the Calabrese et al. (2014) prescription for how the kSZ power spectrum scales with the EoR, we find a 95% CL upper limit on the duration of reionization of $\Delta z_{\text{re}} < 5.4$. Adding the tSZ bispectrum prior from Crawford et al. (2014) strengthens this limit to $\Delta z_{\text{re}} < 4.1$. This 95% confidence upper limit tightens to $\Delta z_{\text{re}} < 3.2$ if the assumed homogeneous kSZ power is increased by 25% ($\sim 0.5 \mu\text{K}^2$) and relaxes to $\Delta z_{\text{re}} < 5.2$ if the homogeneous kSZ power is decreased by the same amount. This supports the recent picture emerging from a number of

sources that reionization happened at late times and fairly quickly.

The SPT is currently being used to conduct a 5 yr survey of 1500 deg² with the SPT-3G camera. The final survey temperature noise levels are expected to be 3, 2, and 9 μ K-arcmin for 95, 150, and 220 GHz, respectively (Bender et al. 2018), which will lead to substantially smaller uncertainties on the power spectrum in all six frequency combinations. Further in the future, the Simons Observatory and CMB-S4 will extend these measurements to larger sky areas, lower noise levels, and more frequency bands (CMB-S4 Collaboration 2019; Simons Observatory Collaboration 2019). Future CMB measurements should tightly constrain the reionization history of the universe.

The South Pole Telescope program is supported by the National Science Foundation through grants PLR-1248097 and OPP-1852617. Partial support is also provided by the NSF Physics Frontier Center grant PHY-0114422 to the Kavli Institute of Cosmological Physics at the University of Chicago, the Kavli Foundation, and the Gordon and Betty Moore Foundation through grant GBMF#947 to the University of Chicago. This work is also supported by the U.S. Department of Energy. S.P. acknowledges support from the Australian Research Council's Discovery Projects scheme (DP150103208). C.R. acknowledges support from Australian Research Council Centre of Excellence for All Sky Astrophysics in 3 Dimensions (ASTRO 3D), through project No. CE170100013. J.W.H. is supported by the National Science Foundation under award No. AST-1402161. W.L.K.W. is supported in part by the Kavli Institute for Cosmological Physics at the University of Chicago through grant NSF PHY-1125897 and an endowment from the Kavli Foundation and its founder Fred Kavli. B.B. is supported by the Fermi Research Alliance LLC under contract No. De-AC02-07CH11359 with the U.S. Department of Energy. The Cardiff authors acknowledge support from the UK Science and Technologies Facilities Council (STFC). The CU Boulder group acknowledges support from NSF AST-0956135. The McGill authors acknowledge funding from the Natural Sciences and Engineering Research Council of Canada, Canadian Institute for Advanced Research, and the Fonds de Recherche du Québec—Nature et technologies. The UCLA authors acknowledge support from NSF AST-1716965 and CSSI-1835865. A.A.S. acknowledges support from NSF AST-1814719. Argonne National Lab, a U.S. Department of Energy Office of Science Laboratory, is operated by UChicago Argonne LLC under contract No. DE-AC02-06CH11357. We also acknowledge support from the Argonne Center for Nanoscale Materials. This research used resources of the National Energy Research Scientific Computing Center (NERSC), a U.S. Department of Energy Office of Science User Facility operated under contract No. DE-AC02-05CH11231. The data analysis pipeline also uses the scientific Python stack (Hunter 2007; Jones et al. 2001; van der Walt et al. 2011) and the HDF5 file format (The HDF Group 1997).

ORCID iDs

C. L. Reichardt  <https://orcid.org/0000-0003-2226-9169>
 S. Patil  <https://orcid.org/0000-0001-5871-7520>
 P. A. R. Ade  <https://orcid.org/0000-0002-5127-0401>
 E. Baxter  <https://orcid.org/0000-0002-6836-3196>
 B. A. Benson  <https://orcid.org/0000-0002-5108-6823>
 F. Bianchini  <https://orcid.org/0000-0003-4847-3483>

L. E. Bleem  <https://orcid.org/0000-0001-7665-5079>
 R. Citron  <https://orcid.org/0000-0001-8920-0356>
 T. M. Crawford  <https://orcid.org/0000-0001-9000-5013>
 M. A. Dobbs  <https://orcid.org/0000-0001-7166-6422>
 W. Everett  <https://orcid.org/0000-0002-5370-6651>
 E. M. George  <https://orcid.org/0000-0001-7874-0445>
 N. Gupta  <https://orcid.org/0000-0001-7652-9451>
 G. P. Holder  <https://orcid.org/0000-0002-0463-6394>
 A. T. Lee  <https://orcid.org/0000-0002-8428-8050>
 S. S. Meyer  <https://orcid.org/0000-0003-3315-4332>
 L. M. Mocuano  <https://orcid.org/0000-0002-2416-2552>
 B. R. Saliwanchik  <https://orcid.org/0000-0002-5089-7472>
 G. Smecher  <https://orcid.org/0000-0002-5560-187X>
 A. A. Stark  <https://orcid.org/0000-0002-2718-9996>
 K. Vanderlinde  <https://orcid.org/0000-0003-4535-9378>
 J. D. Vieira  <https://orcid.org/0000-0001-7192-3871>
 N. Whitehorn  <https://orcid.org/0000-0002-3157-0407>
 W. L. K. Wu  <https://orcid.org/0000-0001-5411-6920>

References

- Austermann, J. E., Aird, K. A., Beall, J. A., et al. 2012, *Proc. SPIE*, 8452, 84521E
- Aylor, K., Hou, Z., Knox, L., et al. 2017, *ApJ*, 850, 101
- Battaglia, N., Bond, J. R., Pfrommer, C., & Sievers, J. L. 2012, *ApJ*, 758, 74
- Battaglia, N., Natarajan, A., Trac, H., Cen, R., & Loeb, A. 2013a, *ApJ*, 776, 83
- Battaglia, N., Trac, H., Cen, R., & Cooray, A. 2013b, *ApJ*, 776, 81
- Bender, A. N., Ade, P. A. R., Ahmed, Z., et al. 2018, *Proc. SPIE*, 10708, 1070803
- Bhattacharya, S., Nagai, D., Shaw, L., Crawford, T., & Holder, G. P. 2012, *ApJ*, 760, 5
- Bocquet, S., Dietrich, J. P., Schrabback, T., et al. 2019, *ApJ*, 878, 55
- Calabrese, E., Hložek, R., Battaglia, N., et al. 2014, *JCAP*, 2014, 010
- Carlstrom, J. E., Ade, P. A. R., Aird, K. A., et al. 2011, *PASP*, 123, 568
- Casey, C. M., Narayanan, D., & Cooray, A. 2014, *PhR*, 541, 45
- CMB-S4 Collaboration 2019, arXiv:1907.04473
- Crawford, T. M., Schaffer, K. K., Bhattacharya, S., et al. 2014, *ApJ*, 784, 143
- Das, S., Louis, T., Nolta, M. R., et al. 2014, *JCAP*, 4, 14
- Das, S., Marriage, T. A., Ade, P. A. R., et al. 2011, *ApJ*, 729, 62
- De Zotti, G., Massardi, M., Negrello, M., & Wall, J. 2010, *A&ARv*, 18, 1
- De Zotti, G., Ricci, R., Mesa, D., et al. 2005, *A&A*, 431, 893
- Dodelson, S., & Schneider, M. D. 2013, *PhRvD*, 88, 063537
- Douspis, M., Salvati, L., & Aghanim, N. 2019, arXiv:1901.05289
- Dunkley, J., Calabrese, E., Sievers, J., et al. 2013, *JCAP*, 7, 25
- Dunkley, J., Hložek, R., Sievers, J., et al. 2011, *ApJ*, 739, 52
- Everett, W. B., Zhang, L., Crawford, T. M., et al. 2020, *ApJ*, 900, 55
- Flender, S., Bleem, L., Finkel, H., et al. 2016, *ApJ*, 823, 98
- George, E. M., Reichardt, C. L., Aird, K. A., et al. 2015, *ApJ*, 799, 177
- Gruzinov, A., & Hu, W. 1998, *ApJ*, 508, 435
- Henning, J. W., Ade, P., Aird, K. A., et al. 2012, *Proc. SPIE*, 8452, 84523A
- Henning, J. W., Sayre, J. T., Reichardt, C. L., et al. 2018, *ApJ*, 852, 97
- Hivon, E., Górski, K. M., Netterfield, C. B., et al. 2002, *ApJ*, 567, 2
- Hou, Z., Aylor, K., Benson, B. A., et al. 2018, *ApJ*, 853, 3
- Hunter, J. D. 2007, *CSE*, 9, 90
- Jones, E., Oliphant, T., Peterson, P., et al. 2001, SciPy: Open Source Scientific Tools for Python, <http://www.scipy.org/>
- Knox, L., Scoccamarro, R., & Dodelson, S. 1998, *PhRvL*, 81, 2004
- Komatsu, E., & Seljak, U. 2002, *MNRAS*, 336, 1256
- Lagache, G., Puget, J.-L., & Dole, H. 2005, *ARA&A*, 43, 727
- Lewis, A., & Bridle, S. 2002, *PhRvD*, 66, 103511
- Lueker, M., Reichardt, C. L., Schaffer, K. K., et al. 2010, *ApJ*, 719, 1045
- Millea, M., Doré, O., Dudley, J., et al. 2012, *ApJ*, 746, 4
- Mocanu, L. M., Crawford, T. M., Aylor, K., et al. 2019, *JCAP*, 2019, 038
- Mocanu, L. M., Crawford, T. M., Vieira, J. D., et al. 2013, *ApJ*, 779, 61
- Padin, S., Staniszewski, Z., Keisler, R., et al. 2008, *ApOpt*, 47, 4418
- Planck Collaboration, Ade, P. A. R., Aghanim, N., et al. 2011, *A&A*, 536, A18
- Planck Collaboration, Ade, P. A. R., Aghanim, N., et al. 2014, *A&A*, 571, A21
- Planck Collaboration, Aghanim, N., Akrami, Y., et al. 2018, *A&A*, 641, A6
- Planck Collaboration, Aghanim, N., Arnaud, M., et al. 2016, *A&A*, 594, A22
- Polenta, G., Marinucci, D., Balbi, A., et al. 2005, *JCAP*, 11, 1
- Reichardt, C. L., Shaw, L., Zahn, O., et al. 2012, *ApJ*, 755, 70
- Remazeilles, M., Bolliet, B., Rotti, A., & Chluba, J. 2019, *MNRAS*, 483, 3459

- Ruhl, J., Ade, P. A. R., Carlstrom, J. E., et al. 2004, [Proc. SPIE](#), **5498**, 11
- Sayre, J. T., Ade, P., Aird, K. A., et al. 2012, [Proc. SPIE](#), **8452**, 845239
- Sehgal, N., Bode, P., Das, S., et al. 2010, [ApJ](#), **709**, 920
- Shang, C., Haiman, Z., Knox, L., & Oh, S. P. 2012, [MNRAS](#), **421**, 2832
- Shaw, L. D., Nagai, D., Bhattacharya, S., & Lau, E. T. 2010, [ApJ](#), **725**, 1452
- Shaw, L. D., Rudd, D. H., & Nagai, D. 2012, [ApJ](#), **756**, 15
- Shirokoff, E., Benson, B. A., Bleem, L. E., et al. 2009, [ITAS](#), **19**, 517
- Shirokoff, E., Reichardt, C. L., Shaw, L., et al. 2011, [ApJ](#), **736**, 61
- Simons Observatory Collaboration 2019, [JCAP](#), **2019**, 056
- Story, K. T., Reichardt, C. L., Hou, Z., et al. 2013, [ApJ](#), **779**, 86
- The HDF Group 1997, [Hierarchical Data Format](#), 5.0
- Tristram, M., Macías-Pérez, J. F., Renault, C., & Santos, D. 2005, [MNRAS](#), **358**, 833
- van der Walt, S., Colbert, S., & Varoquaux, G. 2011, [CSE](#), **13**, 22
- Viero, M. P., Wang, L., Zemcov, M., et al. 2013, [ApJ](#), **772**, 77
- Yue, B., Ferrara, A., Salvaterra, R., Xu, Y., & Chen, X. 2013, [MNRAS](#), **433**, 1556
- Zahn, O., Reichardt, C. L., Shaw, L., et al. 2012, [ApJ](#), **756**, 65